


## Article

# Rational Design of Ratiometric Fluorescent Probe for Zn<sup>2+</sup> Imaging under Oxidative Stress in Cells

Yaheng Li <sup>1,2</sup>, Shankun Yao <sup>1,2</sup>, Hongbao Fang <sup>1,2</sup>, Weijiang He <sup>1,2,3</sup>, Yuncong Chen <sup>1,2,3,\*</sup> and Zijian Guo <sup>1,2,3,\*</sup> 

<sup>1</sup> State Key Laboratory of Coordination Chemistry Coordination Chemistry, School of Chemistry and Chemical Engineering, Nanjing University, Nanjing 210023, China

<sup>2</sup> Chemistry and Biomedicine Innovation Center (ChemBIC), Nanjing University, Nanjing 210023, China

<sup>3</sup> Nanchuang (Jiangsu) Institute of Chemistry and Health, Nanjing 210000, China

\* Correspondence: chenyc@nju.edu.cn (Y.C.); zguo@nju.edu.cn (Z.G.)

**Abstract:** Zn<sup>2+</sup> is a vital ion for most of the physiological processes in the human body, and it usually has a mutual effect with oxidative stress that often occurs in pathological tissues. Detecting fluctuation of Zn<sup>2+</sup> level in cells undergoing oxidative stress could be beneficial to understanding the relationship between them. Herein, a ratiometric fluorescent Zn<sup>2+</sup> probe was rationally designed. The wavelength corresponding to the maximum fluorescence intensity bathometrically shifted from 620 nm to 650 nm after coordinating with Zn<sup>2+</sup>. The intensity ratio of two fluorescence channels changed significantly in cells treated by oxidative stress inducers. It was shown from the results that the labile zinc level was generally elevated under oxidative stress stimulated by various inducers.

**Keywords:** Zn<sup>2+</sup>; oxidative stress; fluorescence imaging; BODIPY; ratiometric probe



**Citation:** Li, Y.; Yao, S.; Fang, H.; He, W.; Chen, Y.; Guo, Z. Rational Design of Ratiometric Fluorescent Probe for Zn<sup>2+</sup> Imaging under Oxidative Stress in Cells. *Chemosensors* **2022**, *10*, 477. <https://doi.org/10.3390/chemosensors10110477>

Academic Editor: Kien Wen Sun

Received: 20 October 2022

Accepted: 8 November 2022

Published: 13 November 2022

**Publisher's Note:** MDPI stays neutral with regard to jurisdictional claims in published maps and institutional affiliations.



**Copyright:** © 2022 by the authors. Licensee MDPI, Basel, Switzerland. This article is an open access article distributed under the terms and conditions of the Creative Commons Attribution (CC BY) license (<https://creativecommons.org/licenses/by/4.0/>).

## 1. Introduction

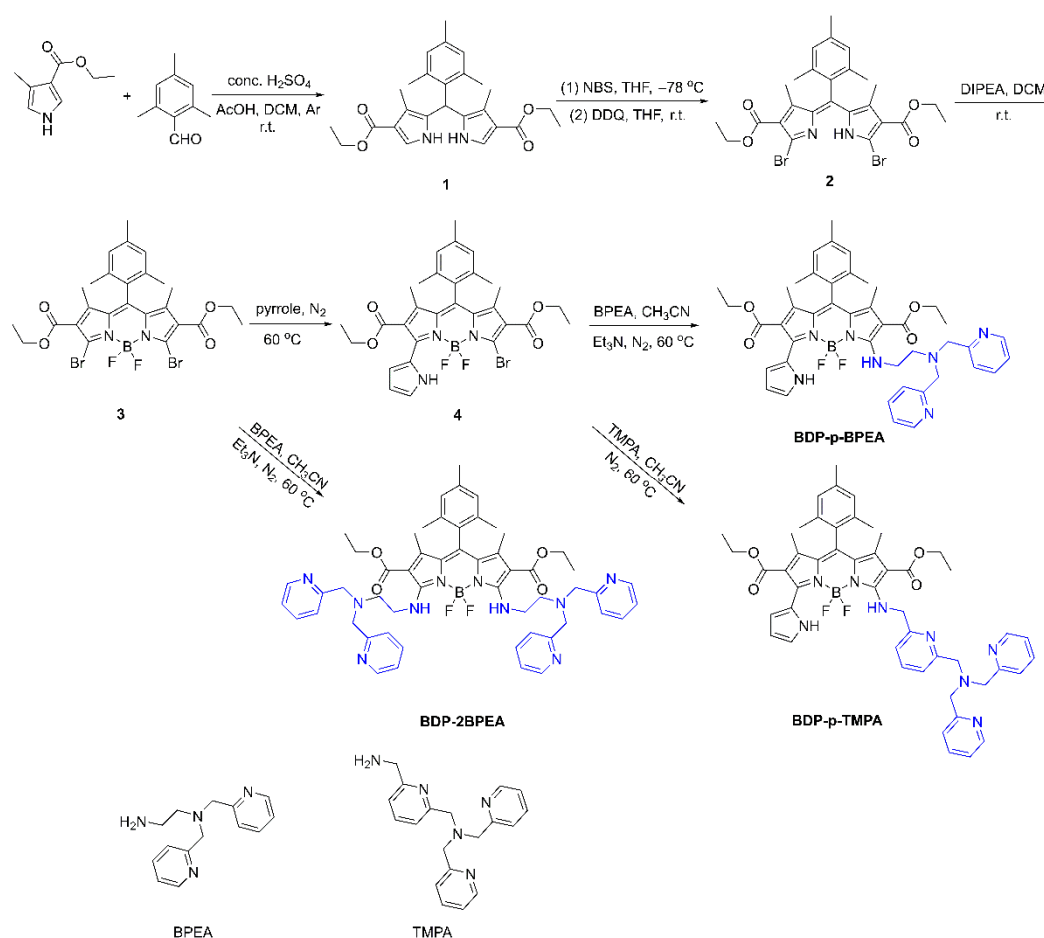
The divalent zinc (Zn<sup>2+</sup>) is crucial for all creatures. In the cellular level, the spatio-temporal distribution of labile zinc has an effect on the process of signal transduction, gene expression, and cell death by adjusting the extent of zinc–protein and/or zinc–nucleus acid combination [1]. As for human beings, Zn<sup>2+</sup> features irreplaceably in numerous biochemical processes, including combining with insulin to guarantee the normal function of pancreas islet [2], inhibiting m-aconitase activity to maintain a high level of citrate in prostate epithelial cells [3], and fluxing during mammalian sperm capacitation to contribute to fertilization [4]. Among them, oxidative stress could be one of the major ways for Zn<sup>2+</sup> to affect cell metabolism [5].

Zn<sup>2+</sup> acts as an anti-oxidant indirectly at a certain concentration range [6], and it also has pro-oxidant effects at both excessively high and low concentration levels [7]. In turn, however, Zn<sup>2+</sup> is released from macromolecules (e.g., metallothionein) during oxidative stress so that the concentration of its labile state elevates [8]. More specifically, if some macromolecules containing Zn<sup>2+</sup> are destroyed to lose their chelating ability by some stimulants, Zn<sup>2+</sup> will be released, which is common in pathological tissues [9–11]. Detecting the Zn<sup>2+</sup> released during this process could be helpful for studying the mutual affection between Zn<sup>2+</sup> and oxidative stress. Furthermore, the extent of impact of Zn<sup>2+</sup>-containing macromolecules induced by different chemicals can be learned from Zn<sup>2+</sup> imaging.

Fluorescence imaging has the merit of good selectivity, sensitivity, and convenience to present the accurate spatio-temporal distribution of analytes, so that it is frequently used to image the metal ion in cells [12]. While there are lots of brilliant materials that can be used as fluorescent sensors to detect metal ions [13–16], small molecule probes stand out among the genetically coded probes and nanoparticle probes by its properties of low toxicity, ease of preparation, and being relatively stable [17]. Currently, satisfactory small molecule fluorescent probes for detecting Zn<sup>2+</sup> in oxidative context are still rare [18–21], mainly because it is challenging to simultaneously consider all of the essential factors such

as selectivity, stability, and prolonging the wavelength of the spectrum. The laser used for excitation should try to be in a visible or near infrared region to avoid extra damage to cells and enhance the signal-to-background ratio during imaging. Moreover, ratiometric probes are preferred in ion detecting occasions since it has a self-calibration effect to prevent many kinds of interference [22].

Based on the fact described above, we synthesized and screened a fluorescent probe to ratiometrically detect  $Zn^{2+}$  in stressed cells. A BODIPY fluorophore was used since it is known to be much more stable and bright in common cell environments [23]. A mesityl group and two methyl groups were introduced to the meso- and  $\beta$ -position separately to prevent rotating induced relaxation, and a pyrrole ring was directly bound to the  $\alpha$ -position of the BODIPY core, so that the wavelengths of both the excitation and emission spectra were prolonged significantly. Among the BODIPY based ratiometric probes, the intramolecular charge transfer (ICT) mechanism was mostly adopted in the designation by locating the recognition group at the 3, 5-position [24], or 8-position [25]. However, this strategy did not always work in the ion-detecting probes because of either the photo-induced electron transfer (PeT) quenching effect or the complexity of the chelating group [26,27]. Therefore, apart from linking a chelating group to the fluorophore, an ester group was added to the ortho-position of the chelating group, which may cause a red shift rather than a blue shift while reacting with a zinc ion [28]. The quantity and position of the ligands were screened to obtain the optimal probe **BDP-p-BPEA**, while another two probes **BDP-p-TMPA** and **BDP-2BPEA** were listed for comparison (Scheme 1).



**Scheme 1.** Synthesis route of the three probes.

## 2. Materials and Methods

### 2.1. Materials and Instruments

All reagents for probe preparation were of analytic grade and purchased from Energy Chemistry (Shanghai, China) and J&K Chemical (Beijing, China). The  $^1\text{H}$  NMR and  $^{13}\text{C}$  NMR spectra were recorded at 25 °C with a Bruker Avance DRX-400 (German) with TMS as the internal reference. High resolution mass spectrometric data were determined using an Agilent 6540Q-TOF HPLC-MS spectrometer (America). The ultrapure water for spectroscopic and cell culture was obtained from a Millipore system (>18.2 M $\Omega$ ). Confocal imaging was performed with a Zeiss LSM710 microscope (German).

### 2.2. Synthesis of Intermediates 1–4 and Probes BDP-2BPEA, BDP-*p*-BPEA, and BDP-*p*-TMPA

#### 2.2.1. Synthesis of 1

To a dichloromethane (16 mL) solution of ethyl 4-methyl-1H-pyrrole-3-carboxylate (3.15 g, 20.5 mmol) were added 33 mL of acetic acid and 0.75 mL of concentrated sulfuric acid under nitrogen atmosphere. After stirring at room temperature for 10 min, 2,4,6-trimethylbenzaldehyde (1.50 g, 10.1 mmol) was added dropwise. The mixture was left to react for 7 h. Upon completion, the solvent was removed by rotary evaporation. Dichloromethane was used to dissolve the residue and the solution was neutralized by a saturated  $\text{NaHCO}_3$  aqueous solution. The aqueous phase was extracted by the same volume of dichloromethane twice. The combined organic phase was dried with  $\text{Na}_2\text{SO}_4$ . The solution of crude product was concentrated and purified by silica gel column chromatography using dichloromethane to dichloromethane/methanol = 4/1 as the eluent to give compound **1** as a white solid (3.31 g, 75.1% yield). MS (ESI+)  $m/z$ : calculated 436.23621; found 437.24182  $[\text{M} + \text{H}]^+$ , 459.22357  $[\text{M} + \text{Na}]^+$ .  $^1\text{H}$  NMR (400 MHz,  $\text{CDCl}_3$ )  $\delta$  7.83 (s, 2H), 7.23 (d,  $J$  = 3.1 Hz, 2H), 6.86 (s, 2H), 5.80 (s, 1H), 4.26 (qd,  $J$  = 7.1, 1.4 Hz, 4H), 2.27 (s, 3H), 1.96 (s, 6H), 1.33 (t,  $J$  = 7.1 Hz, 6H).  $^{13}\text{C}$  NMR (101 MHz,  $\text{CDCl}_3$ )  $\delta$  165.64, 136.94, 136.80, 132.34, 130.91, 127.22, 122.06, 117.15, 116.21, 59.52, 36.07, 20.88, 20.76, 14.63, 10.24.

#### 2.2.2. Synthesis of 2

The synthesis of **2** referred to previously reported literature [29]. Compound **1** (2.00 g, 4.58 mmol) was dissolved into dry tetrahydrofuran (THF, 45 mL) under nitrogen atmosphere, and cooled to  $-78$  °C for more than 10 min. Then, N-bromosuccinimide (1.63 g, 9.16 mmol) was added in three portions every 10 min. After stirring at  $-78$  °C for one hour, 2,3-dichloro-5,6-dicyano-*p*-benzoquinone (1.04 g, 4.58 mmol) was added to the mixture gradually. The mixture reacted for 10 min at  $-78$  °C and was transferred to room temperature and stirred for another 1.5 h. Upon completion, the solvent was evaporated. Forty milliliters of dichloromethane were added, and less soluble components were removed by filtration. The filtrate was concentrated and purified by silica gel column chromatography using petroleum ether/dichloromethane = 2/1 to 0/1 as the eluent to give compound **2** as an orange solid (2.53 g, 93.4% yield). MS (ESI+)  $m/z$ : calculated 592.03954; found 593.04224  $[\text{M} + \text{H}]^+$ , 615.02521  $[\text{M} + \text{Na}]^+$ .  $^1\text{H}$  NMR (400 MHz,  $\text{CDCl}_3$ )  $\delta$  14.13 (s, 1H), 6.96 (s, 2H), 4.28 (q,  $J$  = 7.1 Hz, 4H), 2.34 (s, 3H), 2.05 (s, 6H), 1.60 (s, 6H), 1.34 (t,  $J$  = 7.1 Hz, 6H).  $^{13}\text{C}$  NMR (101 MHz,  $\text{CDCl}_3$ )  $\delta$  163.47, 146.10, 143.79, 139.47, 137.37, 135.10, 131.79, 130.56, 129.55, 121.95, 60.58, 21.36, 19.65, 14.33, 12.43.

#### 2.2.3. Synthesis of 3

To a solution of compound **2** (2.75 g, 4.64 mmol) in 50 mL of dichloromethane was added diisopropylethylamine (4.9 mL, 27.8 mmol). The mixture was stirred for 10 min, and  $\text{BF}_3 \cdot \text{OEt}_2$  (4.8 mL, 37.1 mmol) was dripped into it. The mixture was left to react at room temperature for two hours. Fifteen milliliters of water were added to quench the reaction, and was then neutralized by 1 M NaOH. The aqueous phase was extracted by the same volume of dichloromethane twice. The combined organic phase was dried with  $\text{Na}_2\text{SO}_4$ . The solution of crude product was concentrated and purified by silica gel column chromatography using petroleum ether/dichloromethane = 2/1 to 0/1 as the eluent to give

compound **3** as a red solid (1.96 g, 66.0% yield). MS (ESI+)  $m/z$ : calculated 640.03782; found 641.04327  $[M + H]^+$ , 663.02448  $[M + Na]^+$ .  $^1H$  NMR (400 MHz,  $CDCl_3$ )  $\delta$  7.02 (s, 2H), 4.32 (q,  $J = 7.1$  Hz, 4H), 2.37 (s, 3H), 2.08 (s, 6H), 1.68 (s, 6H), 1.35 (t,  $J = 7.1$  Hz, 6H).  $^{13}C$  NMR (101 MHz,  $CDCl_3$ )  $\delta$  162.63, 147.60, 147.01, 140.45, 134.44, 134.41, 132.50, 130.02, 129.70, 124.68, 61.15, 21.41, 19.68, 14.32, 12.58.

#### 2.2.4. Synthesis of **4**

The synthesis of **4** referred to previously reported literature [30]. Briefly, the mixture of compound **3** (200 mg, 0.31 mmol) and 4 mL of pyrrole was refluxed for 10 h under nitrogen atmosphere. Then, the solvent was removed by rotary evaporation. The crude product was purified by silica gel column chromatography using petroleum ether/dichloromethane = 1/1 to 0/1 as the eluent to give compound **4** as a dark green solid (0.16 g, 82.4% yield). MS (ESI+)  $m/z$ : calculated 625.15591; found 626.16199  $[M + H]^+$ , 648.14520  $[M + Na]^+$ .  $^1H$  NMR (400 MHz,  $CDCl_3$ )  $\delta$  10.59 (br, 1H), 7.20 (m, 1H), 6.99 (s, 2H), 6.86 (m, 1H), 6.36 (dt,  $J = 4.2$ , 2.3 Hz, 1H), 4.32 (p,  $J = 7.1$  Hz, 3H), 2.36 (s, 3H), 2.11 (s, 6H), 1.66 (s, 3H), 1.47 (s, 3H), 1.35 (t,  $J = 7.1$  Hz, 3H), 1.30 (t,  $J = 7.1$  Hz, 3H).  $^{13}C$  NMR (101 MHz,  $CDCl_3$ )  $\delta$  166.02, 163.47, 148.29, 145.48, 141.42, 140.70, 139.82, 135.29, 133.55, 130.58, 130.41, 129.61, 128.13, 126.41, 126.33, 122.35, 121.40, 119.68, 111.64, 61.88, 60.70, 21.39, 19.79, 14.38, 14.15, 12.54, 11.86.

#### 2.2.5. Synthesis of **BDP-2BPEA**

A mixture of compound **3** (100 mg, 0.16 mmol), *N,N*-bis(pyridin-2-ylmethyl)ethane-1,2-diamine (151 mg, 0.62 mmol) and triethylamine (86  $\mu$ L, 0.62 mmol) in 8 mL of acetonitrile was stirred at 60 °C overnight under nitrogen atmosphere. Then, the solvent was removed by rotary evaporation. The crude product was purified by neutral aluminium oxide column chromatography using dichloromethane/ethanol = 100/1 to 20/1 as the eluent to give **BDP-2BPEA** as a blue foam (44 mg, 28.6% yield). MS (ESI+)  $m/z$ : calculated 962.49384; found 963.50043  $[M + H]^+$ , 985.48047  $[M + Na]^+$ .  $^1H$  NMR (400 MHz,  $CDCl_3$ )  $\delta$  8.53 (br, 2H), 8.48 (ddd,  $J = 5.0$ , 1.8, 0.9 Hz, 4H), 7.83 (dt,  $J = 7.8$ , 1.1 Hz, 4H), 7.60 (td,  $J = 7.6$ , 1.8 Hz, 4H), 7.11 (ddd,  $J = 7.5$ , 4.9, 1.2 Hz, 4H), 6.91 (s, 2H), 4.29 (q,  $J = 7.1$  Hz, 4H), 3.96 (t,  $J = 5.9$  Hz, 4H), 3.89 (s, 8H), 2.85 (t,  $J = 5.8$  Hz, 4H), 2.33 (s, 3H), 2.06 (s, 6H), 1.59 (s, 6H), 1.32 (t,  $J = 7.1$  Hz, 6H).  $^{13}C$  NMR (101 MHz,  $CDCl_3$ )  $\delta$  166.54, 159.37, 156.13, 148.87, 142.43, 138.57, 136.67, 136.63, 133.38, 132.67, 128.96, 125.84, 123.52, 122.14, 107.57, 60.18, 60.10, 53.41, 41.62, 21.36, 19.68, 14.53, 12.82.

#### 2.2.6. Synthesis of **BDP-p-BPEA**

A mixture of compound **4** (160 mg, 0.26 mmol), *N,N*-bis(pyridin-2-ylmethyl)ethane-1,2-diamine (93 mg, 0.38 mmol) and triethylamine (53  $\mu$ L, 0.38 mmol) in 10 mL of acetonitrile was stirred at 60 °C for 2 h under nitrogen atmosphere. Then, the solvent was removed by rotary evaporation. The crude product was purified by silica gel column chromatography using dichloromethane/methanol = 1/0 to 10/1 as the eluent to give **BDP-p-BPEA** as a brown solid (130 mg, 63.4% yield). MS (ESI+)  $m/z$ : calculated 787.38289; found 788.38849  $[M + H]^+$ , 810.36523  $[M + Na]^+$ .  $^1H$  NMR (400 MHz,  $CDCl_3$ )  $\delta$  9.98 (br, 1H), 9.06 (br, 1H), 8.52 (d,  $J = 4.9$  Hz, 2H), 7.77 (d,  $J = 7.9$  Hz, 2H), 7.63 (td,  $J = 7.7$ , 1.8 Hz, 2H), 7.16 (ddd,  $J = 7.5$ , 4.8, 1.2 Hz, 2H), 6.95 (s, 3H), 6.62–6.55 (m, 1H), 6.26 (dt,  $J = 3.7$ , 2.6 Hz, 1H), 4.35 (q,  $J = 7.1$  Hz, 2H), 4.20 (q,  $J = 7.1$  Hz, 2H), 4.01 (q,  $J = 5.6$  Hz, 2H), 3.94 (s, 4H), 2.93 (t,  $J = 5.9$  Hz, 2H), 2.34 (s, 3H), 2.09 (s, 6H), 1.71 (s, 3H), 1.44 (s, 3H), 1.35 (t,  $J = 7.1$  Hz, 3H), 1.20 (t,  $J = 7.1$  Hz, 3H).  $^{13}C$  NMR (101 MHz,  $CDCl_3$ )  $\delta$  167.09, 165.87, 158.70, 158.25, 150.21, 148.76, 138.97, 138.75, 136.94, 136.22, 134.83, 133.92, 131.79, 129.75, 129.17, 128.44, 123.72, 122.65, 122.42, 122.37, 119.92, 113.36, 112.53, 109.23, 60.99, 60.77, 59.90, 52.83, 41.69, 21.36, 19.80, 14.40, 14.16, 13.52, 11.26.

#### 2.2.7. Synthesis of **BDP-p-TMPA**

A mixture of compound **4** (140 mg, 0.22 mmol) and 1-(6-(aminomethyl)pyridin-2-yl)-*N,N*-bis(pyridin-2-ylmethyl)methanamine (103 mg, 0.32 mmol) in 10 mL of acetonitrile

was stirred at 60 °C for 1 h under nitrogen atmosphere. Then, the solvent was removed by rotary evaporation. The crude product was purified by silica gel column chromatography using dichloromethane as the eluent to give **BDP-p-TMPA** as a purple foam (164 mg, 86.3% yield). MS (ESI+) *m/z*: calculated 864.40944; found 865.41260 [M + H]<sup>+</sup>, 887.39386 [M + Na]<sup>+</sup>. <sup>1</sup>H NMR (400 MHz, CDCl<sub>3</sub>) δ 10.05 (br, 1H), 10.02 (br, 1H), 8.51 (dt, *J* = 4.9, 1.4 Hz, 2H), 7.67 (t, *J* = 7.6 Hz, 1H), 7.65–7.61 (m, 2H), 7.63–7.56 (m, 2H), 7.50 (d, *J* = 7.6 Hz, 1H), 7.20 (d, *J* = 7.6 Hz, 1H), 7.13 (ddd, *J* = 6.8, 4.9, 1.6 Hz, 2H), 6.98–6.93 (m, 3H), 6.65–6.58 (m, 1H), 6.28 (dt, *J* = 3.7, 2.5 Hz, 1H), 5.20 (d, *J* = 4.5 Hz, 2H), 4.24 (q, *J* = 7.1 Hz, 2H), 4.19 (q, *J* = 7.1 Hz, 2H), 3.99 (s, 2H), 3.94 (s, 4H), 2.35 (s, 3H), 2.11 (s, 6H), 1.73 (s, 3H), 1.46 (s, 3H), 1.25 (t, *J* = 7.3 Hz, 3H), 1.20 (t, *J* = 7.1 Hz, 3H). <sup>13</sup>C NMR (101 MHz, CDCl<sub>3</sub>) δ 167.11, 165.41, 159.56, 158.65, 158.16, 154.68, 150.67, 149.07, 138.92, 138.45, 137.32, 136.60, 136.26, 134.62, 133.48, 131.83, 130.11, 129.14, 128.36, 123.16, 122.77, 122.27, 122.13, 121.84, 120.36, 119.71, 113.17, 113.09, 109.18, 60.93, 60.70, 60.35, 60.12, 49.03, 42.08, 27.12, 25.10, 21.34, 19.82, 14.32, 14.15, 13.53, 11.22.

### 2.3. Optical Experimental Method

Stock solutions of metal ions and probes were prepared by dissolving an appropriate amount in ultrapure water and DMSO, respectively. Solvents for spectroscopic study were of spectral grade from Tedia Company Inc. Absorption spectra were recorded using a PerkinElmer E35 spectrophotometer. Fluorescence spectra were determined using a Horiba FluoroMax-4 spectrofluorometer with the 2 nm and 1 nm slit for excitation and emission, respectively. Excitation wavelength was 550 nm.

The detection limit of three probes were determined according to previous literature [31]. Taking **BDP-p-BPEA** as an example, the fluorescence intensity at 670 nm and 595 nm of the probe was determined 20 times in the identical condition with what was used in the titration experiment. The standard deviation of the twenty  $F_{670}/F_{595}$  value was calculated to be the background noise  $\sigma$ . Then, the limit of detection (LOD) was determined using the following equation:

$$\text{LOD} = \frac{3\sigma}{k}, \text{ k was the slope of the linear fitting curve.}$$

### 2.4. Cell Culture

For oxidative stress inducing experiment, Hela cells were washed by phosphate-buffered saline (PBS) and incubated with 5  $\mu\text{M}$  of probe (in Dulbecco's modified eagle medium, DMEM) for 4 h at 37 °C, followed by washing another 3 times with PBS. Then, 100  $\mu\text{M}$  of 4,4'-dithiodipyridine (DTDP), 50  $\mu\text{M}$  of N-ethylmaleimide (NEM), 50  $\mu\text{M}$  of TPEN, 200  $\mu\text{M}$  of N',N'-diethyl-N-hydroxynitrous hydrazide diethyl ammonium salt (DEA-NONOate) and 20  $\mu\text{M}$  of cisplatin (in DMEM) were added separately to different dishes of cells. Then, the culture dish was put back to incubate for 30 min (for DTDP, NEM and TPEN) or 2 h (for DEA-NONOate and cisplatin), and the cells were washed 3 times with PBS before acquiring the fluorescence image.

The cytotoxicity experiment of **BDP-p-BPEA** in Hela cells was measured using an MTT assay. Cells were seeded into a 96-well cell culture plate at a rate of 4300/well in 5% CO<sub>2</sub> at 37 °C for 24 h, followed by adding probe **BDP-p-BPEA** (0–8  $\mu\text{M}$ ), and then allowed to incubate for 24 h, respectively. Subsequently, each well was injected with 40  $\mu\text{L}$  MTT (2.5 mg/mL) and cultured for another 4 h under the same conditions. Then, the culture medium was removed, and 150  $\mu\text{L}$  of DMSO were added to each well to dissolve the formazan. Absorption of 490 nm of each well was obtained on a microplate reader to indirectly calculate the amount of live cells.

## 3. Results

### 3.1. Design and Synthesis of the Three Probes

The BODIPY core was constructed in a conventional method, that is, aldehyde and two equivalents of pyrrole were condensed and then functionalized by halogenation and

nucleophilic substitution. In this way, we successfully obtained three fluorescent probes that were shown in Scheme 1. All of the newly synthesized compounds were characterized by  $^1\text{H}$  NMR,  $^{13}\text{C}$  NMR, and ESI-MS (Figures S1–S21).

### 3.2. Spectral Response Towards $\text{Zn}^{2+}$ and Screening of the Probes

With three probes in hand, we obtained their absorption spectra in the range of 400–750 nm in acetonitrile/aqueous ( $v/v = 1:1$ ) solution (Figure 1a–c). It can be seen that the absorption bands of **BDP-p-BPEA** and **BDP-p-TMPA** were broad (full width at half maximum were about 100 nm), and the wavelength of maximum absorption changed for 5–10 nm after chelating with  $\text{Zn}^{2+}$ . Thus, their ratiometric absorption turned out to be negligible. As for fluorescence spectra, all of them exhibited ratiometric response to  $\text{Zn}^{2+}$ . **BDP-2BPEA** could chelate with two equivalents of  $\text{Zn}^{2+}$ , and the inflection point at the one equivalent position in the fluorescence titration graph inferred the different electron density distribution on the fluorophore between reacting with one and two equivalents of  $\text{Zn}^{2+}$  (Figure 1d). The fluorescence spectrum of this compound hypochromatically shifted after chelating, regardless of how much  $\text{Zn}^{2+}$  was added. It was supposed that this probe adopted a different binding mode from that of the other two counterparts. In addition, the fluorescence peak of **BDP-p-BPEA** presented the bathochromic shift from 620 nm to 650 nm when reacting with a sufficient amount of  $\text{Zn}^{2+}$  (Figure 1e). When the chelator of the probe was changed to a hexadentate, the bathochromic shift slightly shortened as the electron density change of the ligands that conjugated to fluorophore in average attenuated (Figure 1f). Thus, **BDP-p-BPEA** had a lower detection limit (29 nM) than **BDP-p-TMPA** (41 nM) and **BDP-2BPEA** (50 nM).

Based on the screening results displayed above, the probe **BDP-p-BPEA** was selected to study the optical properties in detail. The probe reached coordination equilibrium with  $\text{Zn}^{2+}$  within 30 s (Figure 2a), and the reversibility, crucial to displaying the dynamic change of  $\text{Zn}^{2+}$  level, was also checked by adding  $\text{ZnCl}_2$  and  $\text{Zn}^{2+}$  scavenger N,N,N',N'-tetrakis(2-pyridinylmethyl)-1,2-ethanediamine (TPEN) solution alternatively to the solution of **BDP-p-BPEA** for five cycles (Figure 2b). The dissociation constant for **BDP-p-BPEA** +  $\text{Zn}^{2+}$  was calculated to be 3.2 nM (Figure S22), providing sufficient affinity for **BDP-p-BPEA** to capture the labile  $\text{Zn}^{2+}$ . Then, the selectivity was tested with common metal ions in the environment (Figure 2c).  $\text{H}_2\text{O}_2$  and its mixture with  $\text{Fe}^{2+}$  were used to mimic oxidative environment in cells. Except for  $\text{Cu}^{2+}$ , all of the tested species negligibly affected the fluorescence response of the probe to  $\text{Zn}^{2+}$ . Fortunately, the  $\text{Cu}^{2+}$  level in cells was too low to compete with the coordination site of the probe with  $\text{Zn}^{2+}$  [32].

### 3.3. Exploring the Sensing Mechanism for **BDP-p-BPEA**

The  $\text{Zn}^{2+}$  binding stoichiometry of **BDP-p-BPEA** was studied by Job's plot and ESI-MS. The fluorescence ratio reached maximum when  $c(\text{BDP-p-BPEA})/([c(\text{BDP-p-BPEA})] + c(\text{BDP-p-BPEA}))$  equaled to 0.5 (Figure 2d); meanwhile, a  $[\text{M} - \text{H} + \text{Zn}]^+$  peak ( $m/z = 850.30214$ ) and a  $[\text{M} + \text{Cl} + \text{Zn}]^+$  peak ( $m/z = 886.27891$ ) were presented in the mass spectrum of **BDP-p-BPEA-Zn $^{2+}$  complex (Figure S23), proving that the probe chelated with  $\text{Zn}^{2+}$  in the manner of 1:1. After that, the  $^1\text{H}$  NMR spectrum of **BDP-p-BPEA** in  $\text{DMSO-}d_6$  before and after being added with  $\text{ZnCl}_2$  were compared (Scheme 2a). We found that three of the H signals of the pyridine rings moved to the lower field, while the H signal of the 3-position of pyridine upshifted. All of the H on the pyrrole ring downshifted because the chelation lowered the electron density of the whole conjugation system. Chemical shift of methylene hydrogen in the chelating group and ester group also changed in different degrees, indicating that the ester group involved in chelating without hydrolysis. In a word, **BDP-p-BPEA** chelated with  $\text{Zn}^{2+}$  in the way showed in Scheme 2b.**

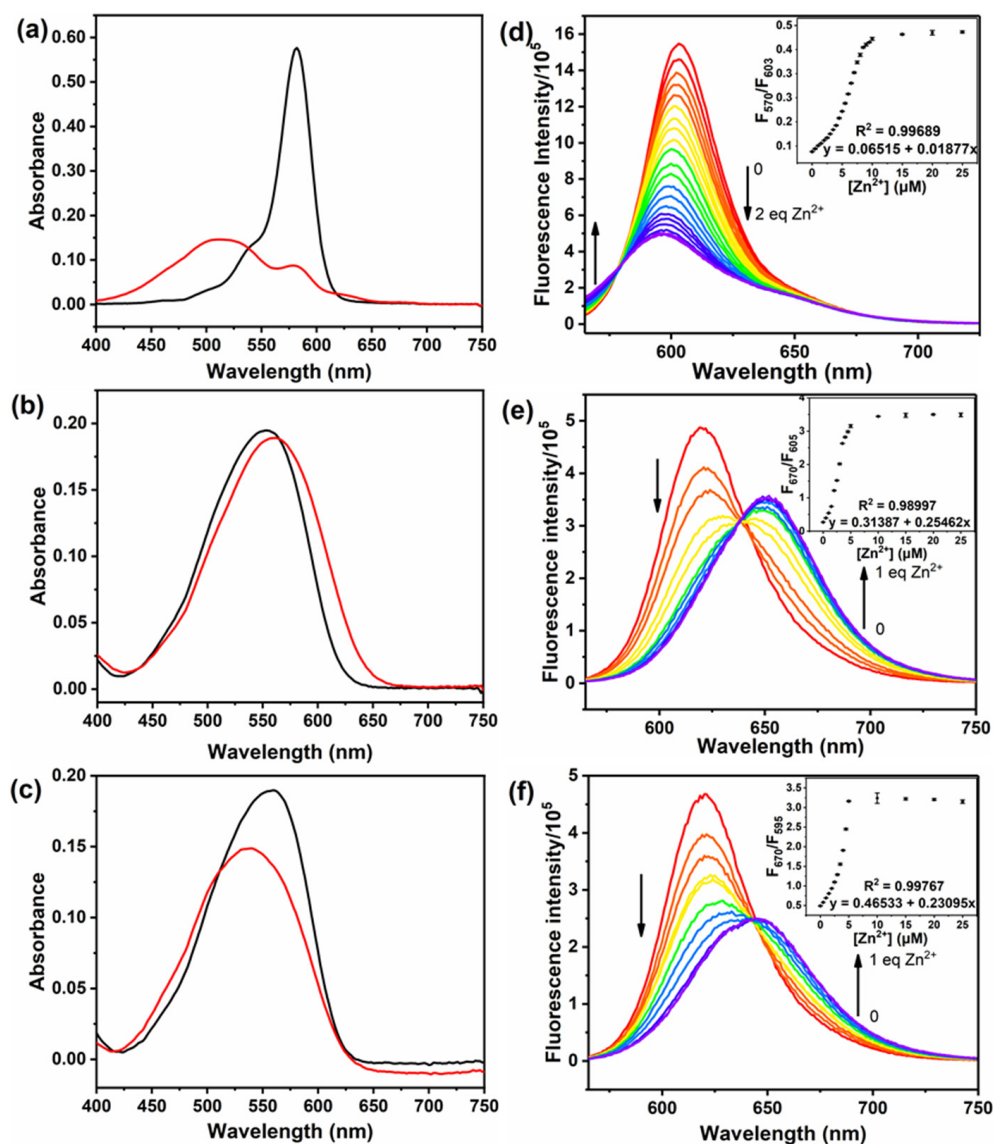


**Figure 1.** (a–c) Absorption spectra of three probes (5 μM) before (black line) and after (red line) being supplemented with ZnCl<sub>2</sub> solution, one equivalent of ZnCl<sub>2</sub> for BDP-p-BPEA and BDP-p-TMPA, and two equivalents for BDP-2BPEA. (a) BDP-2BPEA; (b) BDP-p-BPEA; (c) BDP-p-TMPA; (d–f) fluorescence spectra of three probes (5 μM) titrated with ZnCl<sub>2</sub> solution, λ<sub>ex</sub> = 550 nm; (d) BDP-2BPEA; (e) BDP-p-BPEA; (f) BDP-p-TMPA. All the spectra of the probe were tested in acetonitrile/aqueous media (v/v = 1:1, pH 7.4, 0.05 M HEPES with 0.10 M KNO<sub>3</sub>); Inset: ratio value of fluorescence intensity against the concentration of Zn<sup>2+</sup>, n = 3.

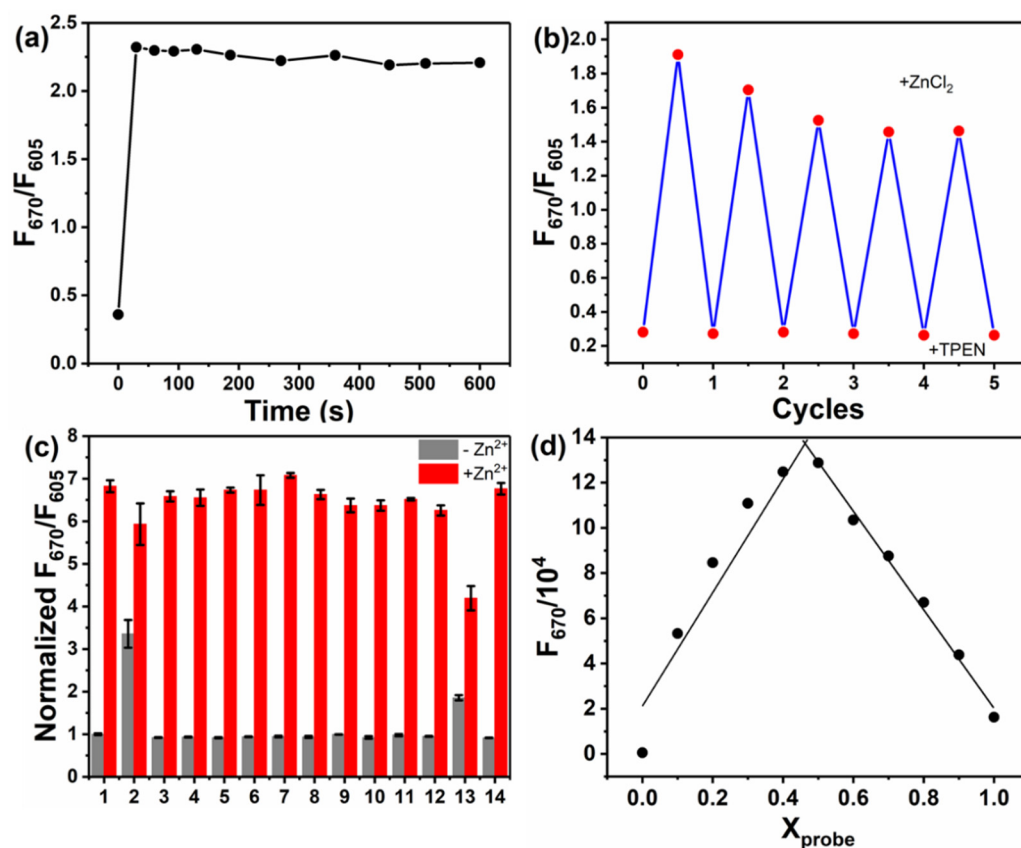
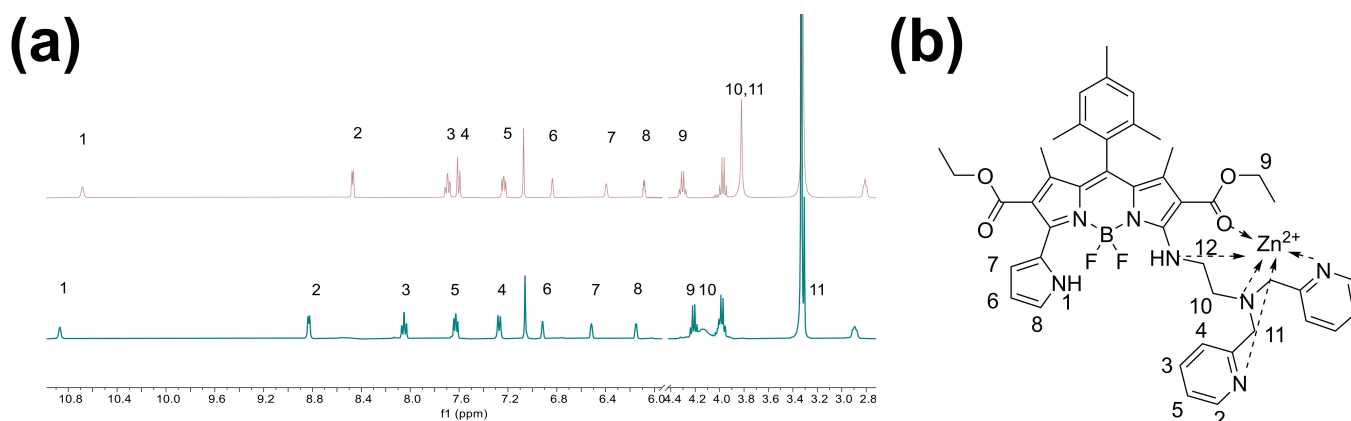


**Figure 2.** Equilibration time, reversibility, and selectivity of **BDP-p-BPEA**. (a) ratio of fluorescence intensity  $F_{670}/F_{605}$  of  $5 \mu\text{M}$  **BDP-p-BPEA** against the time after the addition of  $5 \mu\text{M}$   $\text{ZnCl}_2$ ; (b) ratio of fluorescence intensity  $F_{670}/F_{605}$  of  $5 \mu\text{M}$  **BDP-p-BPEA** with alternative addition of  $5 \mu\text{M}$   $\text{ZnCl}_2$  and TPEN; (c) normalized ratio of fluorescence intensity ( $F_{670}/F_{605}$ )/( $F_{670 \text{ probe}}/F_{605 \text{ probe}}$ ) of  $5 \mu\text{M}$  **BDP-p-BPEA** in the present of 1. blank 2.  $\text{Cu}^{2+}$  3.  $\text{Fe}^{2+}$  4.  $\text{Fe}^{2+} + \text{H}_2\text{O}_2$  5.  $\text{H}_2\text{O}_2$  6.  $\text{Fe}^{3+}$  7.  $\text{Hg}^{2+}$  8.  $\text{Pb}^{2+}$  9.  $\text{Cd}^{2+}$  10.  $\text{Mn}^{2+}$  11.  $\text{Ni}^{2+}$  12. 100 eq  $\text{Na}^+$  +100 eq  $\text{K}^+$  +10 eq  $\text{Ca}^{2+}$  +10 eq  $\text{Mg}^{2+}$  13.  $\text{Co}^{2+}$  14.  $\text{Al}^{3+}$ . All the species were presented as  $5 \mu\text{M}$  (1 eq) if not mentioned,  $n = 3$ ; (d) job's plot of **BDP-p-BPEA**,  $X_{\text{probe}} = c(\text{BDP-p-BPEA})/([\text{Zn}^{2+}] + c(\text{BDP-p-BPEA}))$ , and the total concentration was kept as  $10 \mu\text{M}$ .



**Scheme 2.** (a)  $^1\text{H}$  NMR spectrum (400 MHz) of **BDP-p-BPEA** in  $\text{DMSO-}d_6$  before (up) and after (down) the addition of  $\text{ZnCl}_2$ ; (b) the coordination mode of **BDP-p-BPEA-Zn}^{2+}.**

### 3.4. Imaging of $\text{Zn}^{2+}$ Levels in Cellular Oxidative Stress

As **BDP-p-BPEA** showed great fluorescent response to  $\text{Zn}^{2+}$  in vitro, we next explored its potential to imaging  $\text{Zn}^{2+}$  in cells. The intake of the probe was firstly investigated. The fluorescence intensity in cells gradually enhanced and stopped at 4 h (Figure S24), that



is, it took about 4 h for **BDP-p-BPEA** to reach the balance of intake and outlet. The MTT assay was carried out for three times to make sure the cell viability would not obviously decline while imaging. As a result, the survival rate of HeLa cells kept more than 80% after being treated by 0–8  $\mu\text{M}$  of **BDP-p-BPEA** for 24 h (Figure S25), so the cytotoxicity was evaluated to be low enough to apply the probe to cell imaging. Interested about the cell distribution of the probe, we co-stained **BDP-p-BPEA** with mitochondrial, lysosome, endoplasmic reticulum (ER), Golgi apparatus, and lipid droplet targeting commercial dyes separately. As shown in Figure 3, **BDP-p-BPEA** mainly distributed in lipid droplet and ER, and other organelles were also stained in varied degrees. This property enabled us to observe the overall fluctuation of  $\text{Zn}^{2+}$  level in cells.

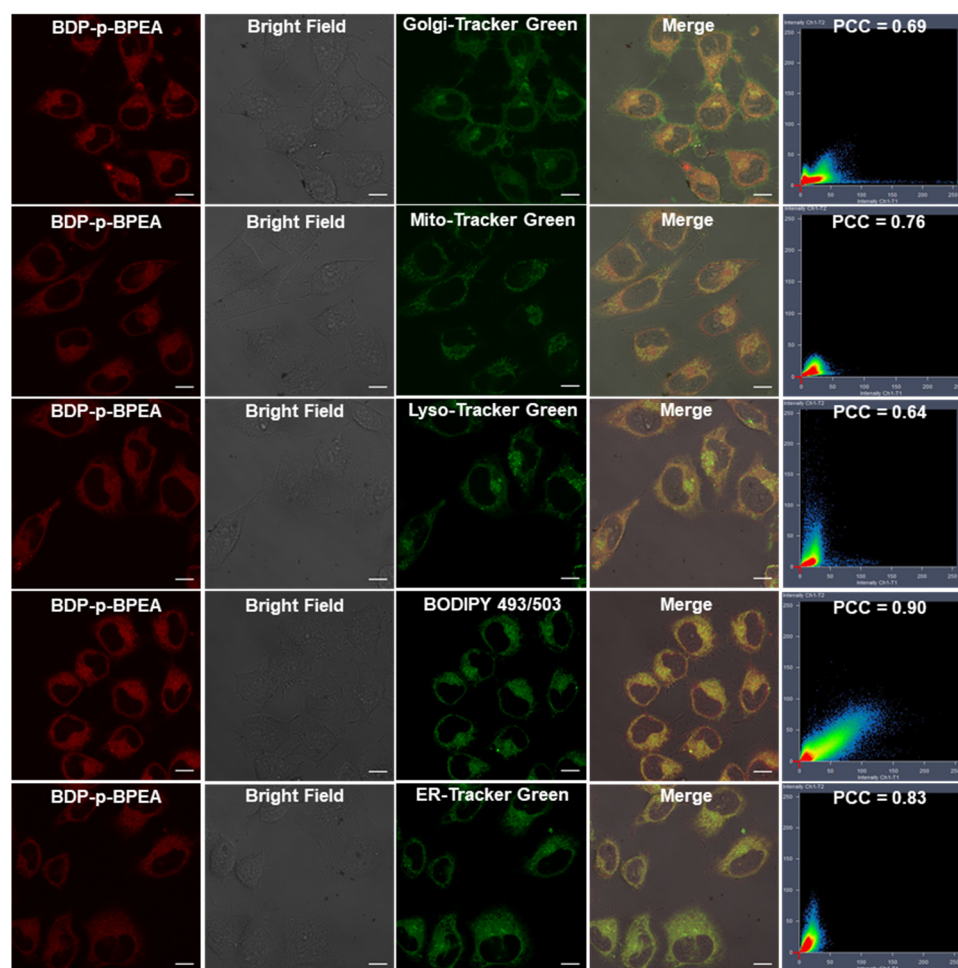


**Figure 3.** The colocalization experiment of **BDP-p-BPEA** with Mito-Tracker Green, Lyso-Tracker Green, ER-Tracker Green, Golgi-Tracker Green and lipid droplet targeting commercial dye BODIPY 493/503, respectively. For **BDP-p-BPEA**,  $\lambda_{\text{ex}} = 543 \text{ nm}$ ,  $\lambda_{\text{em}} = 570\text{--}615 \text{ nm}$ , for commercial dyes,  $\lambda_{\text{ex}} = 488 \text{ nm}$ ,  $\lambda_{\text{em}} = 500\text{--}550 \text{ nm}$ , scale bar: 10  $\mu\text{m}$ .

Cells fully stained with **BDP-p-BPEA** exhibited a bright fluorescence signal, so we tried to determine the variation of  $\text{Zn}^{2+}$  levels in stress induced by different mechanisms using **BDP-p-BPEA**. Cisplatin and scavenger of biothiols—DTDP and NEM were used to treat HeLa cells. All the reagents listed above were reported to cause oxidative stress at certain concentrations [33–35]. Nitric oxide, provided by DEA-NONOate, reacted with metalloproteins, which not only released  $\text{Zn}^{2+}$  from storage, but also had a close relationship with the formation of oxidative stress [36,37]. Therefore, it was also adopted to treat HeLa cells. We used a ratio graph to show the relative intensity change of the two channels more clearly. The results in Figure 4 showed that NO, DTDP and cisplatin significantly raised ratio value, while NEM induced a relatively low increase. The results indicated that

oxidative stress easily converted  $Zn^{2+}$  from a tightly-binding state to labile state. TPEN made the ratio value slightly lower than that of the control group, and it means the original endogenous labile zinc can be detected by **BDP-p-BPEA**. As a result, it was disclosed with **BDP-p-BPEA** that the labile  $Zn^{2+}$  level was elevated during oxidative stress.

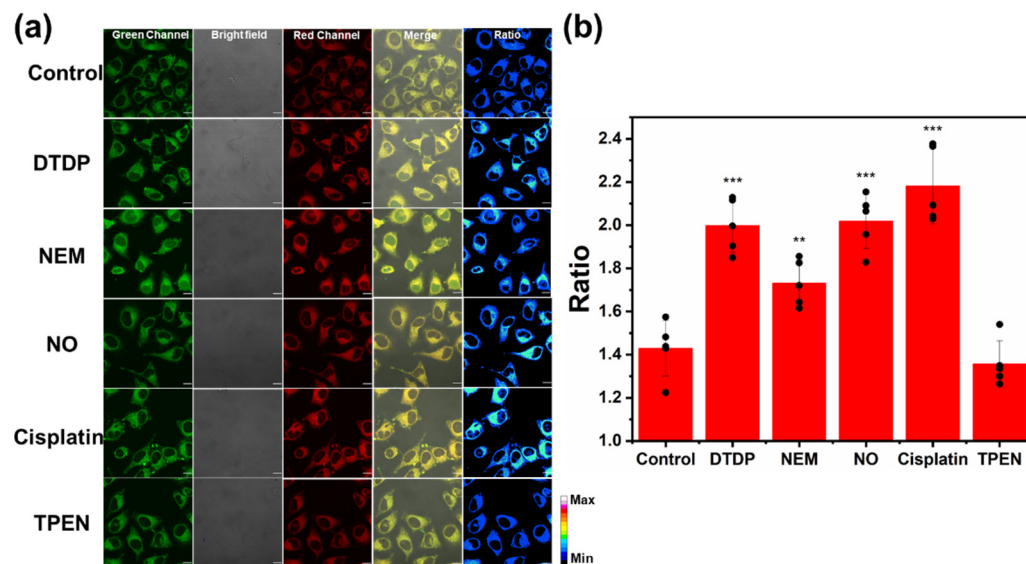


**Figure 4.** (a) Cells incubated with 5  $\mu$ M **BDP-p-BPEA** for four hours and supplemented with DTDP, NEM, TPEN (for 0.5 h), DEA-NONOate, and cisplatin (for 2 h) separately before acquiring fluorescence imaging. Green Channel = 570–615 nm, red channel = 650–720 nm, scale bar: 10  $\mu$ m; (b) average fluorescence ratio value of cells in each graph, ratio =  $F_{red}/F_{green}$ , \*\*  $p < 0.01$  and \*\*\*  $p < 0.001$ .

### 3.5. Comparison with the Previous Methods

Many fluorescent  $Zn^{2+}$  probes have been designed up to now, and some representative ones were listed below (Table 1). Though cyanine and hemicyanine based probes had excellent hydrophilicity and near infrared absorption, they seldom performed ratiometric responses to  $Zn^{2+}$  [21,38]. Meanwhile, the cyanine structure was fragile to destruction from reactive oxygen species. The combination of coumarin and other fluorophores could be made as a ratiometric probe based on a fluorescence resonance energy transfer (FRET) mechanism [39,40], but they had higher LOD value and had to be excited by a near ultraviolet laser, which may cause extra damage to cells while imaging. Currently, most of the BODIPY based  $Zn^{2+}$  probes blueshifted after their coordination with  $Zn^{2+}$  [41], while **BDP-p-BPEA** presented a redshift response. It was a pity that a large part of the probes could not simultaneously solve the problems of sensitivity [42], solubility in water [43], and short wavelength [44]. The probe proposed in this work showed great sensitivity, selectivity, and ratiometric response to  $Zn^{2+}$ , so it has better imaging performance than other  $Zn^{2+}$  probes to some extent.

**Table 1.** Performance comparison between **BDP-p-BPEA** and other  $Zn^{2+}$  probes.

Detection Mode	$\lambda_{ex}$ (nm)/ $\lambda_{em}$ (nm)	Fluorophore	Linear Range ( $\mu M$ )	LOD (nM)	Testing Media	$K_d$ (nM)	Ref.
Enhanced	750/779	cyanine	0.1–5.0	11	25 mM HEPES	$1.42 \times 10^3$	[21]
Enhanced	687/703	hemicyanine	0–1.4	0.45	HEPES buffer solution (10 mM, pH 7.0)	$1.05 \times 10^3$	[38]
Ratiometric	415/560 to 480	coumarin & benzo[c][1,2,5]oxadiazole	0–5	82	DMSO: aqueous solution (50 mM HEPES 100 mM $KNO_3$ , pH = 7.40) $v:v = 1:99$	0.014	[39]
Enhanced	390/460	coumarin & rhodamine	0–10	$3.2 \times 10^2$	0.1 M Tris, pH 7.4	$3.94 \times 10^3$	[40]
Ratiometric	610 to 575/700 to 660	BODIPY	0–10	31.8	DMSO: aqueous solution (50 mM HEPES 100 mM $KNO_3$ , pH = 7.2) $v:v = 3:2$	3.65	[41]
Ratiometric	430 to 475/660	isophorone	0–8	106	DMSO: aqueous solution (10 mM HEPES, pH = 7.46) $v:v = 1:1$	$7.7 \times 10^3$	[42]
Enhanced	544 to 607/634	dipyrrolyldipyrrin	(No data)	210	DMF	13	[43]
Enhanced	346/414	naphthalimide	0–0.003	0.047	DMSO: aqueous solution (10 mM HEPES, pH 7.4) $v:v = 1:9$	4.70	[44]
Ratiometric	550/620 to 650	BODIPY	0–3	29	MeCN: aqueous solution (50 mM HEPES 100 mM $KNO_3$ , pH 7.4) $v:v = 1:1$	3.2	This work

#### 4. Conclusions

To sum up, we synthesized and screened a ratiometric fluorescent  $Zn^{2+}$  probe with a stable structure, and it was capable of imaging in the oxidative environment. Its maximum fluorescence signal moved from 620 nm to 650 nm after chelating. Brilliant optical properties were obtained to image the fluctuation of labile zinc in Hela cells undergoing oxidative stress. In addition, cisplatin induced elevation of  $Zn^{2+}$  level in cells was also observed. The probe showed its potential to be used in super-resolution imaging in the future by virtue of its spectra of relatively long wavelength and stability, we will consider modifying the structure of **BDP-p-BPEA** to further prolong its wavelength so that it can be applied to in vivo  $Zn^{2+}$  imaging of inflammatory tissues, where oxidative stress frequently occurs.

**Supplementary Materials:** The following supporting information can be downloaded at: <https://www.mdpi.com/article/10.3390/chemosensors10110477/s1>, Figure S1: ESI-MS spectra of **1**; Figure S2:  $^1H$  NMR spectra of **1**; Figure S3:  $^{13}C$  NMR spectra of **1**; Figure S4: ESI-MS spectra of **2**; Figure S5:  $^1H$  NMR spectra of **2**; Figure S6:  $^{13}C$  NMR spectra of **2**; Figure S7: ESI-MS spectra of **3**; Figure S8:  $^1H$  NMR spectra of **3**; Figure S9:  $^{13}C$  NMR spectra of **3**; Figure S10: ESI-MS spectra of **4**; Figure S11:  $^1H$  NMR spectra of **4**; Figure S12:  $^{13}C$  NMR spectra of **4**; Figure S13: ESI-MS spectra of **BDP-2BPEA**; Figure S14:  $^1H$  NMR spectra of **BDP-2BPEA**; Figure S15:  $^{13}C$  NMR spectra of **BDP-2BPEA**; Figure S16: ESI-MS spectra of **BDP-p-BPEA**; Figure S17:  $^1H$  NMR spectra of **BDP-p-BPEA**; Figure S18:  $^{13}C$  NMR spectra of **BDP-p-BPEA**; Figure S19: ESI-MS spectra of **BDP-p-TMPA**; Figure S20:  $^1H$  NMR spectra of **BDP-p-TMPA**; Figure S21:  $^{13}C$  NMR spectra of **BDP-p-TMPA**; Figure S22: The Hill plot of **BDP-p-BPEA** complexation with  $Zn^{2+}$ ; Figure S23: ESI-MS spectra of **BDP-p-BPEA** +  $Zn^{2+}$ ; Figure S24: (a) confocal imaging of Hela cells treated by **BDP-p-BPEA** for 1–4 h; (b) average fluorescence intensity of cells in green channel of each graph. Green channel = 570–615 nm, red channel = 650–720 nm, scale bar: 10  $\mu m$ ; Figure S25: Viability of Hela cells versus the concentration of **BDP-p-BPEA**.

**Author Contributions:** Conceptualization, investigation, data curation and writing—original draft preparation, Y.L.; validation and formal analysis, S.Y.; writing—review and editing, H.F.; supervision and project administration, Y.C.; funding acquisition and resources, W.H., Y.C., and Z.G. All authors have read and agreed to the published version of the manuscript.

**Funding:** Z.G. was funded by the National Natural Science Foundation of China (21731004, 92153303, 91953201), the Natural Science Foundation of Jiangsu Province (BK20202004), and the Excellent Research Program of Nanjing University (ZYJH004). Y.C. was funded by the National Natural Science Foundation of China (22122701, 21907050) and the Natural Science Foundation of Jiangsu Province (BK20190282). W.H. was funded by the National Natural Science Foundation of China (21977044). H.F. was funded by the National Postdoctoral Program for Innovative Talents (BX2021123), the China Postdoctoral Science Foundation (2021M691505), and the Jiangsu Postdoctoral Research Funding Program (2021K125B).

**Institutional Review Board Statement:** Not applicable.

**Informed Consent Statement:** Not applicable.

**Data Availability Statement:** The data presented in this study are available on request from the corresponding author.

**Conflicts of Interest:** The authors declare no conflict of interest.

## References

1. Valko, M.; Jomova, K.; Rhodes, C.J.; Kuča, K.; Musílek, K. Redox- and non-redox-metal-induced formation of free radicals and their role in human disease. *Arch. Toxicol.* **2016**, *90*, 1–37. [[CrossRef](#)] [[PubMed](#)]
2. Li, Y.V. Zinc and insulin in pancreatic beta-cells. *Endocrine* **2014**, *45*, 178–189. [[CrossRef](#)] [[PubMed](#)]
3. Costello, L.C.; Franklin, R.B. A comprehensive review of the role of zinc in normal prostate function and metabolism; and its implications in prostate cancer. *Arch. Biochem. Biophys.* **2016**, *611*, 100–112. [[CrossRef](#)] [[PubMed](#)]
4. Kerns, K.; Zigo, M.; Drobnis, E.Z.; Sutovsky, M.; Sutovsky, P. Zinc ion flux during mammalian sperm capacitation. *Nat. Commun.* **2018**, *9*, 2061. [[CrossRef](#)]
5. Paithankar, J.G.; Saini, S.; Dwivedi, S.; Sharma, A.; Chowdhuri, D.K. Heavy metal associated health hazards: An interplay of oxidative stress and signal transduction. *Chemosphere* **2021**, *262*, 128350. [[CrossRef](#)]
6. Yuan, Y.; Niu, F.; Liu, Y.; Lu, N. Zinc and its effects on oxidative stress in Alzheimer's disease. *Neurol. Sci.* **2014**, *35*, 923–928. [[CrossRef](#)]
7. Maret, W. The redox biology of redox-inert zinc ions. *Free Radical Bio. Med.* **2019**, *134*, 311–326. [[CrossRef](#)]
8. Marreiro, D.d.N.; Climaco Cruz, K.J.; Silva Morais, J.B.; Beserra, J.B.; Severo, J.S.; Soares de Oliveira, A.R. Zinc and oxidative stress: Current mechanisms. *Antioxidants* **2017**, *6*, 24. [[CrossRef](#)]
9. Aizenman, E.; Stout, A.K.; Hartnett, K.A.; Dineley, K.E.; McLaughlin, B.; Reynolds, I.J. Induction of neuronal apoptosis by thiol oxidation: Putative role of intracellular zinc release. *J. Neurochem.* **2000**, *75*, 1878–1888. [[CrossRef](#)]
10. Hao, Q.; Maret, W. Aldehydes release zinc from proteins. A pathway from oxidative stress/lipid peroxidation to cellular functions of zinc. *FEBS J.* **2006**, *273*, 4300–4310. [[CrossRef](#)]
11. McCord, M.C.; Aizenman, E. The role of intracellular zinc release in aging, oxidative stress, and Alzheimer's disease. *Front. Aging Neurosci.* **2014**, *6*, 77. [[CrossRef](#)] [[PubMed](#)]
12. Wang, F.; Wang, K.; Kong, Q.; Wang, J.; Xi, D.; Gu, B.; Lu, S.; Wei, T.; Chen, X. Recent studies focusing on the development of fluorescence probes for zinc ion. *Coord. Chem. Rev.* **2021**, *429*, 213636. [[CrossRef](#)]
13. Lin, Y.; Yang, Z.; Lake, R.J.; Zheng, C.; Lu, Y. Enzyme-mediated endogenous and bioorthogonal control of a DNAzyme fluorescent sensor for imaging metal ions in living cells. *Angew. Chem. Int. Ed.* **2019**, *58*, 17061–17067. [[CrossRef](#)] [[PubMed](#)]
14. Zhang, Y.; Xu, S.; Li, X.; Zhang, J.; Sun, J.; Tong, L.; Zhong, H.; Xia, H.; Hua, R.; Chen, B. Improved LRET-based detection characters of Cu<sup>2+</sup> using sandwich structured NaYF<sub>4</sub>@NaYF<sub>4</sub>:Er<sup>3+</sup>/Yb<sup>3+</sup>@NaYF<sub>4</sub> nanoparticles as energy donor. *Sens. Actuators B Chem.* **2018**, *257*, 829–838. [[CrossRef](#)]
15. Dong, H.; Zhao, L.; Chen, Y.; Li, M.; Chen, W.; Wang, Y.; Wei, X.; Zhang, Y.; Zhou, Y.; Xu, M. Dual-ligand near-infrared luminescent lanthanide-based metal-organic framework coupled with in vivo microdialysis for highly sensitive ratiometric detection of Zn<sup>2+</sup> in a mouse model of Alzheimer's disease. *Anal. Chem.* **2022**, *94*, 11940–11948. [[CrossRef](#)]
16. Liu, R.; Kowada, T.; Du, Y.; Amagai, Y.; Matsui, T.; Inaba, K.; Mizukami, S. Organelle-level labile Zn(2+) mapping based on targetable fluorescent sensors. *ACS Sens.* **2022**, *7*, 748–757. [[CrossRef](#)]
17. Jiang, X.; Wang, L.; Carroll, S.L.; Chen, J.; Wang, M.C.; Wang, J. Challenges and opportunities for small-molecule fluorescent probes in redox biology applications. *Antioxid. Redox. Signal.* **2018**, *29*, 518–540. [[CrossRef](#)]
18. Hagimori, M.; Hara, F.; Mizuyama, N.; Fujino, T.; Saji, H.; Mukai, T. High-affinity ratiometric fluorescence probe based on 6-amino-2,2'-bipyridine scaffold for endogenous Zn(2+) and its application to living cells. *Molecules* **2022**, *27*, 1287. [[CrossRef](#)]

19. Hu, Z.; Yang, G.; Hu, J.; Wang, H.; Eriksson, P.; Zhang, R.; Zhang, Z.; Uvdal, K. Real-time visualizing the regulation of reactive oxygen species on Zn<sup>2+</sup> release in cellular lysosome by a specific fluorescent probe. *Sensor. Actuat. B Chem.* **2018**, *264*, 419–425. [[CrossRef](#)]
20. Zhu, H.; Fan, J.; Zhang, S.; Cao, J.; Song, K.; Ge, D.; Dong, H.; Wang, J.; Peng, X. Ratiometric fluorescence imaging of lysosomal Zn(2+) release under oxidative stress in neural stem cells. *Biomater. Sci.* **2014**, *2*, 89–97. [[CrossRef](#)]
21. Xiao, H.; Li, P.; Zhang, S.; Zhang, W.; Zhang, W.; Tang, B. Simultaneous fluorescence visualization of mitochondrial hydrogen peroxide and zinc ions in live cells and in vivo. *Chem. Commun.* **2016**, *52*, 12741–12744. [[CrossRef](#)] [[PubMed](#)]
22. Trusso Sfrassetto, G.; Satriano, C.; Tomaselli, G.A.; Rizzarelli, E. Synthetic fluorescent probes to map metallostasis and intracellular fate of zinc and copper. *Coord. Chem. Rev.* **2016**, *311*, 125–167. [[CrossRef](#)]
23. Liu, M.; Ma, S.; She, M.; Chen, J.; Wang, Z.; Liu, P.; Zhang, S.; Li, J. Structural modification of BODIPY: Improve its applicability. *Chin. Chem. Lett.* **2019**, *30*, 1815–1824. [[CrossRef](#)]
24. Deniz, E.; Isbasar, G.C.; Bozdemir, Ö.A.; Yildirim, L.T.; Siemiarczuk, A.; Akkaya, E.U. Bidirectional switching of near IR emitting boradiazaindacene fluorophores. *Org. Lett.* **2008**, *10*, 3401–3403. [[CrossRef](#)]
25. Hiruta, Y.; Koiso, H.; Ozawa, H.; Sato, H.; Hamada, K.; Yabushita, S.; Citterio, D.; Suzuki, K. Near IR Emitting red-shifting ratiometric fluorophores based on borondipyrromethene. *Org. Lett.* **2015**, *17*, 3022–3025. [[CrossRef](#)]
26. Bozdemir, O.A.; Guliyev, R.; Buyukcakar, O.; Selcuk, S.; Kolemen, S.; Gulseren, G.; Nalbantoglu, T.; Boyaci, H.; Akkaya, E.U. Selective manipulation of ICT and PET processes in styryl-bodipy derivatives: Applications in molecular logic and fluorescence sensing of metal ions. *J. Am. Chem. Soc.* **2010**, *132*, 8029–8036. [[CrossRef](#)]
27. Guliyev, R.; Ozturk, S.; Kostereli, Z.; Akkaya, E.U. From virtual to physical: Integration of chemical logic gates. *Angew. Chem. Int. Ed.* **2011**, *50*, 9826–9831. [[CrossRef](#)]
28. Xia, S.; Shen, J.; Wang, J.; Wang, H.; Fang, M.; Zhou, H.; Tanasova, M. Ratiometric fluorescent and colorimetric BODIPY-based sensor for zinc ions in solution and living cells. *Sensor. Actuat. B Chem.* **2018**, *258*, 1279–1286. [[CrossRef](#)]
29. Kawashima, H.; Ukai, S.; Nozawa, R.; Fukui, N.; Fitzsimmons, G.; Kowalczyk, T.; Fliegl, H.; Shinokubo, H. Determinant factors of three-dimensional aromaticity in antiaromatic cyclophanes. *J. Am. Chem. Soc.* **2021**, *143*, 10676–10685. [[CrossRef](#)]
30. Dai, E.; Pang, W.; Zhang, X.F.; Yang, X.; Jiang, T.; Zhang, P.; Yu, C.; Hao, E.; Wei, Y.; Mu, X.; et al. Synthesis and photophysics of BF<sub>2</sub>-rigidified partially closed chain bromotetrapyrroles: Near infrared emitters and photosensitizers. *Chem. Asian. J.* **2015**, *10*, 1327–1334. [[CrossRef](#)]
31. Zhang, S.; Adhikari, R.; Fang, M.; Dorh, N.; Li, C.; Jaishi, M.; Zhang, J.; Tiwari, A.; Pati, R.; Luo, F.T.; et al. Near-infrared fluorescent probes with large Stokes shifts for sensing Zn(II) ions in living cells. *ACS Sens.* **2016**, *1*, 1408–1415. [[CrossRef](#)] [[PubMed](#)]
32. Rae, T.D.; Schmidt, P.J.; Pufahl, R.A.; Culotta, V.C.; O'Halloran, T.V. Undetectable intracellular free copper: The requirement of a copper chaperone for superoxide dismutase. *Science* **1999**, *284*, 805–808. [[CrossRef](#)] [[PubMed](#)]
33. Malaiyandi, L.M.; Dineley, K.E.; Reynolds, I.J. Divergent consequences arise from metallothionein overexpression in astrocytes: Zinc buffering and oxidant-induced zinc release. *Glia* **2004**, *45*, 346–353. [[CrossRef](#)] [[PubMed](#)]
34. Kannan, N.; Nguyen, L.V.; Makarem, M.; Dong, Y.; Shih, K.; Eirew, P.; Raouf, A.; Emerman, J.T.; Eaves, C.J. Glutathione-dependent and -independent oxidative stress-control mechanisms distinguish normal human mammary epithelial cell subsets. *Proc. Natl. Acad. Sci. USA* **2014**, *111*, 7789–7794. [[CrossRef](#)]
35. Yu, W.; Chen, Y.; Dubrulle, J.; Stossi, F.; Putluri, V.; Sreekumar, A.; Putluri, N.; Baluya, D.; Lai, S.Y.; Sandulache, V.C. Cisplatin generates oxidative stress which is accompanied by rapid shifts in central carbon metabolism. *Sci. Rep.* **2018**, *8*, 4306. [[CrossRef](#)]
36. Chang, C.J.; Jaworski, J.; Nolan, E.M.; Sheng, M.; Lippard, S.J. A tautomeric zinc sensor for ratiometric fluorescence imaging Application to nitric oxide-induced release of intracellular zinc. *Proc. Natl. Acad. Sci. USA* **2003**, *101*, 1129–1134. [[CrossRef](#)]
37. Wei, T.; Chen, C.; Hou, J.; Xin, W.; Mori, A. Nitric oxide induces oxidative stress and apoptosis in neuronal cells. *Biochim. Biophys. Acta* **2000**, *1498*, 72–79. [[CrossRef](#)]
38. Fang, M.; Xia, S.; Bi, J.; Wigstrom, T.P.; Valenzano, L.; Wang, J.; Tanasova, M.; Luck, R.L.; Liu, H. Detecting Zn(II) ions in live cells with near-infrared fluorescent probes. *Molecules* **2019**, *24*, 1592. [[CrossRef](#)]
39. Xu, H.; Zhu, C.; Chen, Y.; Bai, Y.; Han, Z.; Yao, S.; Jiao, Y.; Yuan, H.; He, W.; Guo, Z. A FRET-based fluorescent Zn(2+) sensor: 3D ratiometric imaging, flow cytometric tracking and cisplatin-induced Zn(2+) fluctuation monitoring. *Chem. Sci.* **2020**, *11*, 11037–11041. [[CrossRef](#)]
40. Wang, X.; Bai, X.; Su, D.; Zhang, Y.; Li, P.; Lu, S.; Gong, Y.; Zhang, W.; Tang, B. Simultaneous fluorescence imaging reveals N-methyl-D-aspartic acid receptor dependent Zn(2+)/H(+) flux in the brains of mice with depression. *Anal. Chem.* **2020**, *92*, 4101–4107. [[CrossRef](#)]
41. Fang, H.; Li, Y.; Yao, S.; Geng, S.; Chen, Y.; Guo, Z.; He, W. An endoplasmic reticulum-targeted ratiometric fluorescent molecule reveals Zn(2+) micro-dynamics during drug-induced organelle ionic disorder. *Front. Pharmacol.* **2022**, *13*, 927609. [[CrossRef](#)] [[PubMed](#)]
42. Feng, J.; Li, J.Z.; Mao, X.M.; Wang, Q.; Li, S.P.; Wang, C.Y. Real-time detection and imaging of exogenous and endogenous Zn(2+) in the PC12 cell model of depression with a NIR fluorescent probe. *Analyst* **2021**, *146*, 3971–3976. [[CrossRef](#)] [[PubMed](#)]

43. Miao, W.; Dai, E.; Sheng, W.; Yu, C.; Hao, E.; Liu, W.; Wei, Y.; Jiao, L. Direct synthesis of dipyrrolyldipyrins from SNAr reaction on 1,9-dihalodipyrins with pyrroles and their NIR fluorescence “turn-on” response to  $Zn^{2+}$ . *Org. Lett.* **2017**, *19*, 6244–6247. [[CrossRef](#)] [[PubMed](#)]
44. Fang, L.; Trigiane, G.; Crespo-Otero, R.; Hawes, C.S.; Philpott, M.P.; Jones, C.R.; Watkinson, M. Endoplasmic reticulum targeting fluorescent probes to image mobile  $Zn^{2+}$ . *Chem. Sci.* **2019**, *10*, 10881–10887. [[CrossRef](#)] [[PubMed](#)]